Shear TEsting Programme: Cosmic shear analysis of image simulations

Catherine Heymans[1], Ludovic Van Waerbeke, Richard Massey, David Bacon, Gary Bernstein, Emmanuel Bertin, Sarah Bridle, Michael L. Brown, Douglas Clowe, Håkon Dahle, Thomas Erben, Meghan Gray, Marco Hetterscheidt, Henk Hoekstra, Mike Jarvis, Konrad Kuijken, Vera Margoniner, Yannick Mellier, Reiko Nakajima, Molly Peeples, Alexandre Refregier, Jason Rhodes, Tim Schrabback, David Wittman.

Abstract

The Shear TEsting Programme, STEP, can improve the accuracy and reliability of all weak lensing measurements through the rigorous testing of cosmic shear pipelines, the exchange of data and the sharing of technical knowledge. In this report we present the STEP analysis of sheared image simulations, comparing the results obtained from different shear measurement methods. For all but two of the authors this shear measurement was performed without knowledge of the input simulation shear. The most successful method over a wide range of shear distortions $0 < \gamma < 0.1$ was found to be the Hoekstra implementation of KSB, which produces results that are accurate to better than the 2% level. Similarly accurate results are found in the weak $\gamma < 0.01$ regime with the Bernstein & Jarvis technique. Overall there is an interesting scatter in the results that reveals both residual PSF distortions and calibration bias in some, but not all, methods. In most cases PSF systematics are successfully below the 0.1% level, although the accuracy of the PSF correction is found to be strongly dependent on the form of the PSF distortion. Calibration errors from real data cannot be detected through diagnostic tests such as an E/B mode decomposition and so our finding that shear calibration is often only accurate to $\sim 10\%$ (or worse) in $\sim 50\%$ of the methods tested, causes some concern. Different implementations of the KSB formalism produces remarkably different results and so we provide details of different KSB cosmic shear pipelines to aid the improvement of future KSB analyses. Alternative methods to KSB and Bernstein & Jarvis, appear to fare only as well (or worse) when compared to the average results of the commonly used KSB method. We determine the accuracy of source detection, measure centroid errors and determine levels of selection bias and weight bias. We also investigate the dependence of shear measurements on galaxy properties such as magnitude and size. For some methods we can conclude that the measured calibration bias is related to selection bias and/or the use of biased weights. For other methods the calibration biases appear to arise from the measurement method itself.

[1]Max-Planck-Institut für Astronomie. e-mail: heymans@mpia.de

1 Introduction

Cosmic shear is a unique probe of the dark matter distribution and has the great promise of being able to constrain the properties of dark energy. The weak shear signal is however technically very difficult to measure. The Shear TEsting Programme, (STEP), was therefore initially launched to see how accurately members of the weak lensing community could measure cosmic shear from a set of sheared image simulations using a variety of different techniques, as listed in Table 1.

Author	Institute	Key	Method	σ_8 (?)
Sarah Bridle	UCL	SB	im2shape [Bridle et al., 2001]	
Michael Brown	Edinburgh	MB	KSB (Bacon pipeline) Massey uses identical pipeline	0.74 ± 0.09 1.09 ± 0.12
Douglas Clowe	Steward	C1 & C2	KSB	
Hakon Dahle	ITA, Oslo	HD	K2K [Kaiser, 2000]	
Meghan Gray	Nottingham	MG	KSB	
Marco Hetterscheidt	Bonn	MH	KSB (Erben pipeline)	
Catherine Heymans	MPIA	CH	KSB	0.68 ± 0.12
Henk Hoekstra	UVic	HH	KSB	$0.86^{+0.09}_{-0.13}$
Mike Jarvis	UPenn	MJ	Bernstein and Jarvis [2002] Rounding kernel method	$0.71^{+0.12}_{-0.16}$
Konrad Kuijken	Leiden	KK	Shapelets to 8^{th} order [Refregier and Bacon, 2003]	
Vera Margoniner	Davis	VM	Wittman et al. [2000]	
Reiko Nakajima	UPenn	RN	Bernstein and Jarvis [2002] Matrix inversion method	
Jason Rhodes	JPL	JR	Rhodes et al. [2000]	1.02 ± 0.16
Tim Schrabback	Bonn	TS	KSB (Erben+ pipeline)	
Ludovic Van Waerbeke	UBC	LV	KSB	0.83 ± 0.07

Table 1: Table of authors and methods. The key identifies the authors in all future plots and tables. The authors most recent constraints on σ_8 are also listed for reference where $\Omega_m = 0.3$ [Brown et al., 2003, Heymans et al., 2004, Hoekstra et al., 2002, Jarvis et al., 2003, Massey et al., 2004, Rhodes et al., 2004, Van Waerbeke et al., 2004].

The primary STEP goal has been to investigate two types of systematic error in cosmic shear analysis; the presence of residual instrumental distortions after PSF correction, and the presence of calibration bias. Diagnostic statistics allow us to decompose cosmic shear signals into their lensing E-modes and non-lensing B-modes [Brown et al., 2003, Crittenden et al., 2002, Schneider et al., 2002], immediately alerting us to the presence of residual instrumental distortions within our data sets. A B-mode detection can be reduced through the modification of PSF models or merely the selection of angular scales above/below which the systematics are low. Calibration bias is therefore perhaps of greater concern as in contrast to PSF-related errors, it can only be detected through the cosmic shear analysis of image simulations. This analysis also allows us to investigate the accuracy of source detection methods, measure centroid errors, and determine selection bias and weight bias all of which can add additional error into cosmological parameter estimation from cosmic shear measurements.

In this report, organised as follows, we present the results of the blind[2] STEP analysis of two different types of sheared image simulations. In section 2 we briefly describe the SkyMaker and shapelets simulation data and the different types of analysed PSFs. We concentrate initially on the SkyMaker

[2]CH and LV knew the input shear of the SkyMaker simulations. RM knew the input of the shapelets simulations.

simulations, in section 3, comparing each authors measured shear to the input simulation shear. We measure the level of calibration bias and PSF contamination for each type of PSF analysed in section 3.1. We then match the catalogues to the input catalogues in Section 3.2 to investigate the impact of false detections in each analysis and measure the PSF dependent centroid errors. To determine levels of selection bias, in section 3.3, we compare the measured shear signal with the mean shear calculated from the selected galaxies input shear, and assess the impact of weighting schemes in section 3.4. In section 4 we present the results of the analysis of the shapelet simulations comparing each authors measured shear to the input simulation shear. We focus on the most commonly used KSB analysis in section 5 and attempt to detail the key differences between each authors implementation of this method. A summary of the alternative methods to KSB is given in section 6. Note that this report does include all key plots but for a fuller analysis, readers are requested to use this report in conjunction with the supplementary material provided. We conclude in section 7 but note that any explanation of our findings will be intimately linked to the differences between individual authors cosmic shear pipelines and we therefore defer the interpretation of these results to a future date.

2 STEP Simulation data

2.1 SkyMaker simulations

The SkyMaker programme[3] generates images of galaxies modelled as exponential disks with a central de Vaucouleurs type bulge of varying ratio (see Erben et al. 2001 for details). Model galaxy images are then convolved with a series of realistic ground-based PSFs. Each STEP simulation set is an ensemble of 64 4096×4096 pixel images of pixel scale 0.206 arcsecs with roughly 15 galaxies per square arcminute for each set. A set of fixed shears, listed in Table 2, has been applied to each simulation set and each set has been convolved with 6 different isotropic PSFs listed in Table 3 and shown in the upper panel of Figure 1. Although the PSF was known to be isotropic across the field of view, isotropy has only been assumed in one case (RN).

nlens	γ_1	γ_2
0	0.0	0.0
1	0.005	0.0
2	0.01	0.0
3	0.05	0.0
4	0.1	0.0

Table 2: Input shear values for the SkyMaker simulations

PSF ID	seeing	PSF type
0	0.9	no anisotropy
1	0.7	coma in arcsec (0.4 0.3)
2	0.7	jitter in arcsec (major axis 0.4 minor axis 0.3 angle +30)
3	0.7	defocusing 0.4 arcsec
4	0.7	astigmatism in arcsec (0.4 0.3)
5	0.7	triangular PSF in arcsec (0.4 0.3)

Table 3: The SkyMaker simulations are convolved with this series of isotropic PSF models

[3] http://terapix.iap.fr/cplt/oldSite/soft/skymaker

2.2 Shapelet simulations

The shapelet simulations differ from the SkyMaker simulations by including different galaxy morphology. Objects in COSMOS[4] images are parametrised in shapelet space and this distribution is then used to generate a population of galaxies (see Massey et al. 2004 for more details). These shapelet model galaxies are then convolved with differing PSFs, shown in the lower panel of figure 1, to simulate ground-based observations. The applied shears are listed in Appendix Table 7.

3 Analysis of SkyMaker simulations

In this section we compare each authors measured shear catalogues with the input to each SkyMaker simulation. For the SkyMaker simulations we treat each image as an independent data set and measure (weighted) quantities, such as the mean shear or mean centroid error, in each of the 64 images that form a set with constant PSF distortion and external shear. We then take the quantity to be the mean of the measurements from the 64 images and assign an error to that quantity given by the error on the mean.

3.1 Calibration bias and PSF contamination

We measure the degree of offset between each authors measured shear and the input shear, listed in table 2, as a function of PSF type. The supplementary material `KSB_analysis.ps` and `other_analysis.ps` shows the difference between the measured shear and the true shear for each PSF type and each author, split into two groups; those who use the KSB technique (discussed in more detail in section 5) and those who use alternative techniques (summarised in section 6). For each author and PSF we determine the best-fit parameters to

$$\gamma_1 - \gamma_1^{\rm true} = q(\gamma_1^{\rm true})^2 + m_1\gamma_1^{\rm true} + c_1 \tag{1}$$

where we would expect $m_1 = 0$ in the absence of calibration bias, $c_1 = 0$ in the absence of PSF systematics, and $q = 0$ for a linear response of the method to shear. In the case where the fitted parameter q is consistent with zero, we re-fit with a simple linear relationship. For all SkyMaker simulations $\gamma_2 = 0$ and we therefore find the best-fitting straight line relationship to

$$\gamma_2 = m_2\gamma_1^{\rm true} + c_2 \tag{2}$$

where we would expect $m_2 = 0$ in the absence of selection bias and $c_2 = 0$ in the absence of PSF systematics.

Figure 2 shows each authors best fitting value for $|m_1|$, $|c_1|$, $|m_2|$ and $|c_2|$, for PSF types 0-2, and Figure 3 shows the same for PSF types 3-5. For the cases where $q \neq 0$, denoted with a circle, the best-fit q parameter is shown with respect to the right-hand scale. **In short, the lower the result on the y axis, the lower the level of calibration bias, and the further the result is placed to the left, the lower the level of PSF contamination. The higher the q value the poorer the response to stronger shear.** When the m and c fitted parameters are found to be consistent with zero an arrow is shown, otherwise errors on the fits are shown in the direction of the best case scenario of lower calibration bias, and lower PSF contamination.

Results consistently accurate to $< 2\%$ were found with the Hoekstra (HH) implementation of KSB. Similarly high accuracy is found in the limit $\gamma \leq 0.01$ by both implementations of Bernstein and Jarvis [2002] (MJ,RN). At higher shear however this methodology breaks down which can be seen from the high q values. All KSB implementations are accurate to better than 15% but the spread in results that use essentially the same method is disconcerting. The Kuijken implementation of shapelets (KK) [Refregier and Bacon, 2003] (KK), the Dahle implementation of K2K (HD) [Kaiser, 2000] and the

[4]www.astro.caltech.edu/∼cosmos

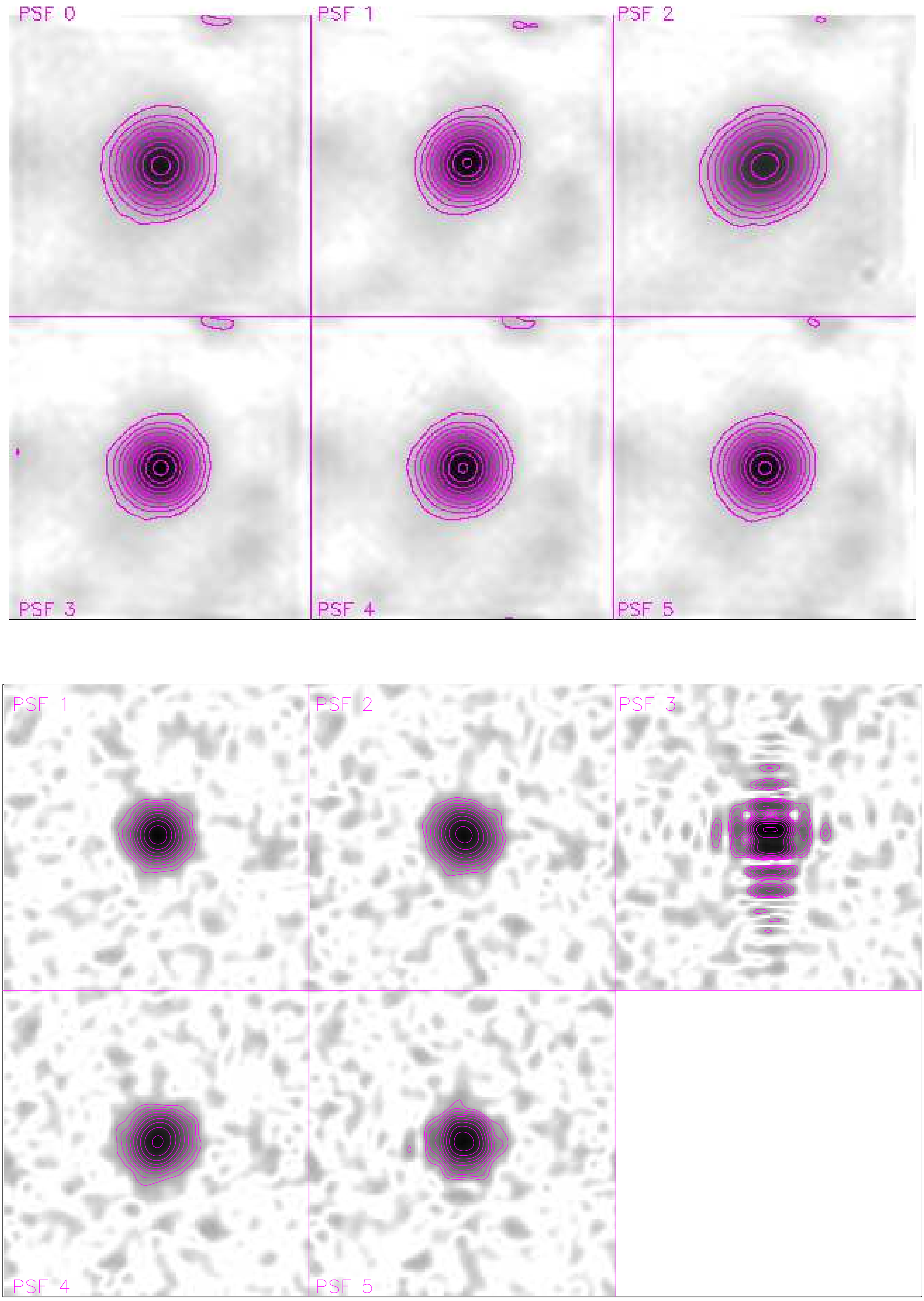

Figure 1: Stacked stellar images, shown here on a log-grey-scale, show the different types of simulated PSF distortion. Each box spans $\sim 6.5 \times 6.5$ arcsecs. The upper panel shows the SkyMaker simulation PSFs, as described in Table 3, and the lower panel shows the shapelet simulation PSFs.

Wittman/Margoniner method(VM) (see section 6.5) all suffer from calibration bias at $\sim 10\%$ or higher. im2shape [Bridle et al., 2001] (SB) typically fares as well as the Brown (MB) implementation of KSB with an accuracy of $\sim 5\%$. In general PSF contamination was successfully removed to below the 0.1% level except in the cases of PSF 1 (coma) and PSF 2 (jitter) which caused the most problems for the complete removal of PSF distortions leaving residuals below the 1% level.

3.2 Shot noise, source detection and centroid errors

The accuracy of shear measurements are closely linked to the accuracy of the source detection, the accuracy of the source centroid measurements, and the minimisation of shot noise. Different methods use different source selection criteria to maximise source counts and minimise source detection errors. A significant number of false detections and stellar contamination will, in principle, add noise that dilutes the average shear measurement and with the presence of systematic centroiding errors there is the potential for centroid bias in the final result [Bernstein and Jarvis, 2002, Kaiser, 2000].
Most methods use the *SExtractor* software [Bertin and Arnouts, 1996] to detect objects and determine their centroid positions where the *SExtractor* analysis parameters that have been used are detailed in Table 4. Hoekstra (HH), Brown (MB) and Gray (MG) use the peak finding tool *hfindpeaks* from the *imcat*[5] software. We match galaxies in each measured catalogue to the input galaxy catalogue, within a tolerance of 5 pixels. Appendix tables 8 and 9 list the number density of detected sources, which can be compared to the input source density of ~ 15 galaxies per square arcmin. The signal-to-noise ratio is then measured for different PSFs with the highest signal-to-noise (by far) resulting from the two implementations of the Bernstein and Jarvis [2002] method (MJ,RN). The percentage of false (or unmatched galaxy) detections are also listed which often result from stellar contamination. Typically the proportion of false galaxy detections are below 5%, with as few as $\leq 1\%$ false galaxy detections with the methods of Van Waerbeke (LV), Schrabback (TS) and Nakajima. The method Dahle (HD) has strong stellar contamination which can be improved upon in future analyses.

author	DETECT_MINAREA	DETECT_THRESH	FILTER_NAME
C1&C2	3	1.0	gauss_3.0_7x7.conv
MH	4	1.2	gauss_4.0_7x7.conv
CH	11	1.5	tophat_3.0_3x3.conv
MJ	5	1.2	gauss_4.0_7x7.conv
KK	5	1.5	default.conv
VM	6	2.0	default.conv
RN	5	1.0	gauss_3.0_5x5.conv
JR	5	1.5	gauss_5.0_9x9.conv
TS	4	1.2	gauss_4.0_7x7.conv

Table 4: SExtractor parameters

The supplementary `shear_from_real_false_detections.ps` shows the shear measured from the real (black) and false (orange) detections. For many methods, false detections contribute random noise with a measured shear $<\gamma^{\rm false}>\sim 0$. This will weakly dilute the signal in proportion to the percentage of false detections in the catalogues. In the cases of Bridle (SB), Margoniner (VM), Nakajima (RN),

[5] *www.ifa.hawaii.edu/∼kaiser/imcat/*

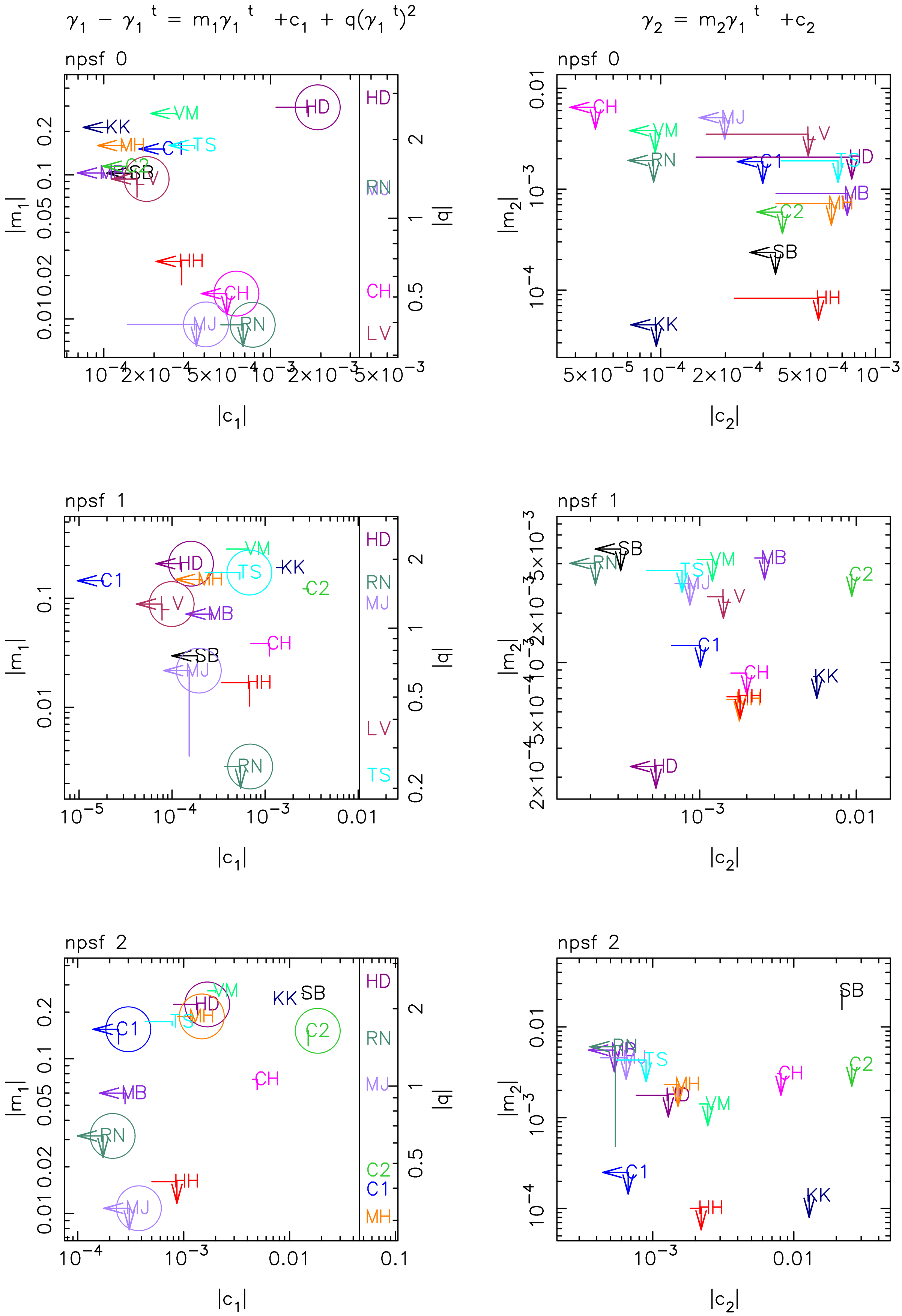

Figure 2: The best fitting values for m_1, c_1 and q (equation 1) and m_2 and c_2 (equation 2) for each author (key listed in table 1), for PSF types 0-2. For the cases where $q \neq 0$, denoted with a circle, the best-fit q parameter is shown with respect to the right-hand scale. Errors are plotted in the direction that reduces m_i and c_i to zero except in the cases when parameters are consistent with zero where an arrow is shown.

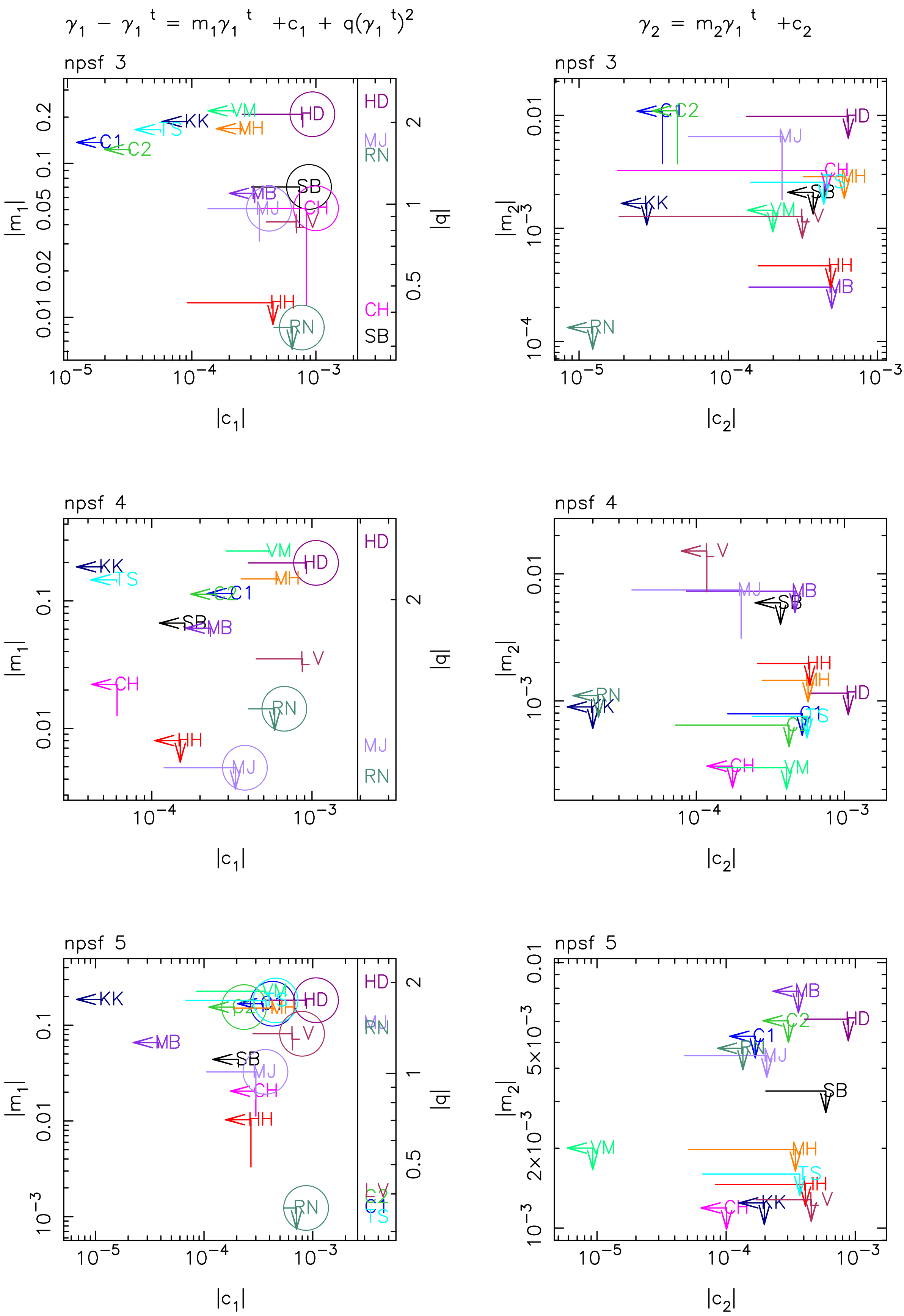

Figure 3: The best fitting values for m_1, c_1 and q (equation 1) and m_2 and c_2 (equation 2) for each author (key listed in table 1), for PSF types 3-5. For the cases where $q \neq 0$, denoted with a circle, the best-fit q parameter is shown with respect to the right-hand scale. Errors are plotted in the direction that reduces m_i and c_i to zero except in the cases when parameters are consistent with zero where an arrow is shown.

Clowe (C1&2), Hetterscheidt (MH), Hoekstra (HH) and Schrabback (TS) (TS), false detections have a significant shear measure (typically $\sim 1-2\%$) that will weakly bias the average shear measured from the full catalogue. Note that after submission Clowe inspected some of the object detection catalogues by eye to reject double objects, stellar spikes (although the PSFs did not include spider reflections), and so on. This resulted in the rejection of $\sim 5\%$ of the objects increasing the shear by $\sim 5\%$. These false objects also effected the weighting scheme used in the Clowe (C1&2) analysis.
From the matched catalogues we measure the average offset between the measured centroid position and input position. We find an offset of ~ -0.5 pixels with most authors who use *hfindpeaks* which arises from differing definitions of the (0,0) position in a fits image. We find that the centroid error is not dependent on the external shear applied to the image but is sensitive to the PSF used. Figure 4 shows that the centroid offsets for each author using *SExtractor* are typically better than 0.001 pixels. For those using *hfindpeaks*, centroids are are accurate to 0.01 pixels (after including a 0.5 pixel shift). Exceptions occur for PSF 1 (coma) where most authors are ~ 1 pixel off. Centroid offsets and errors are given in the Appendix, Tables 8 and 9. Note the Hoekstra (HH) centroid offset results from the truncating format of the catalogue.

3.3 Selection Bias

When compiling source catalogues one should consider selection bias. Preference by source extraction software to select galaxies oriented in the same direction as the PSF [Kaiser, 2000] and galaxies that are anti-correlated with the gravitational shear (and as a result appear more circular) [Hirata and Seljak, 2003], would bias the mean ellipticity of the population. Selection criteria applied after source extraction could also bias the mean ellipticity of the population if the selection has any dependence on galaxy shape. In this section we measure the unweighted mean shear from the 'real' galaxies in each authors measured shear catalogues, inserting the input galaxy shear instead of the author measured shear. We define the input galaxy 'shear' to be

$$\begin{pmatrix} \gamma_1 \\ \gamma_2 \end{pmatrix} = \frac{1-\beta}{1+\beta} \begin{pmatrix} \cos 2\theta \\ \sin 2\theta \end{pmatrix}, \tag{3}$$

where β is the axial ratio of the ellipse and θ is the position angle (see Bartelmann and Schneider 2001 section 4.2 for different definitions of galaxy ellipticity and the relationship to galaxy shear). We combine the shear of the bulge and disk component with a ratio that is proportional to the bulge-to-total flux ratio. We perform the same analysis as section 3 and compare the mean input shear with the (weighted) mean measured shear for the same set of selected 'real' galaxies. Figure 5 compares the offset parameter m_1 from equation 1 measured from author selected galaxies using the input galaxy shears (x axis) and the measured galaxy shears (y axis). **In short, the lower the result on the y axis, the lower the level of measured calibration bias, and the further the result is placed to the left, the lower the level of selection bias (with no selection bias $m = 0$). With unbiased measurement methods, points should fall along the 1:1 line plotted.** Note that any preference to select galaxies oriented with the direction of the PSF (measured with the c parameter from equation 1) was not seen. Selection bias $\sim 5\%$ can be seen in the methods of Clowe (C1&2), Schrabback (TS), Dahle (HD) and Nakajima (RN). With most authors however the selection bias is below the $\sim 1\%$ level and is often consistent with zero bias. These methods use both the *SExtractor* and *hfindpeaks* source extraction algorithms which leads us to deduce that the selection bias seen with other methods is likely to result from specific selection criteria not from the source extraction software. Comparing the position of each point relative to the 1:1 relationship shows that the calibration bias seen in the measured results cannot be simply attributed to selection bias and that therefore measurement bias exists within some methods.

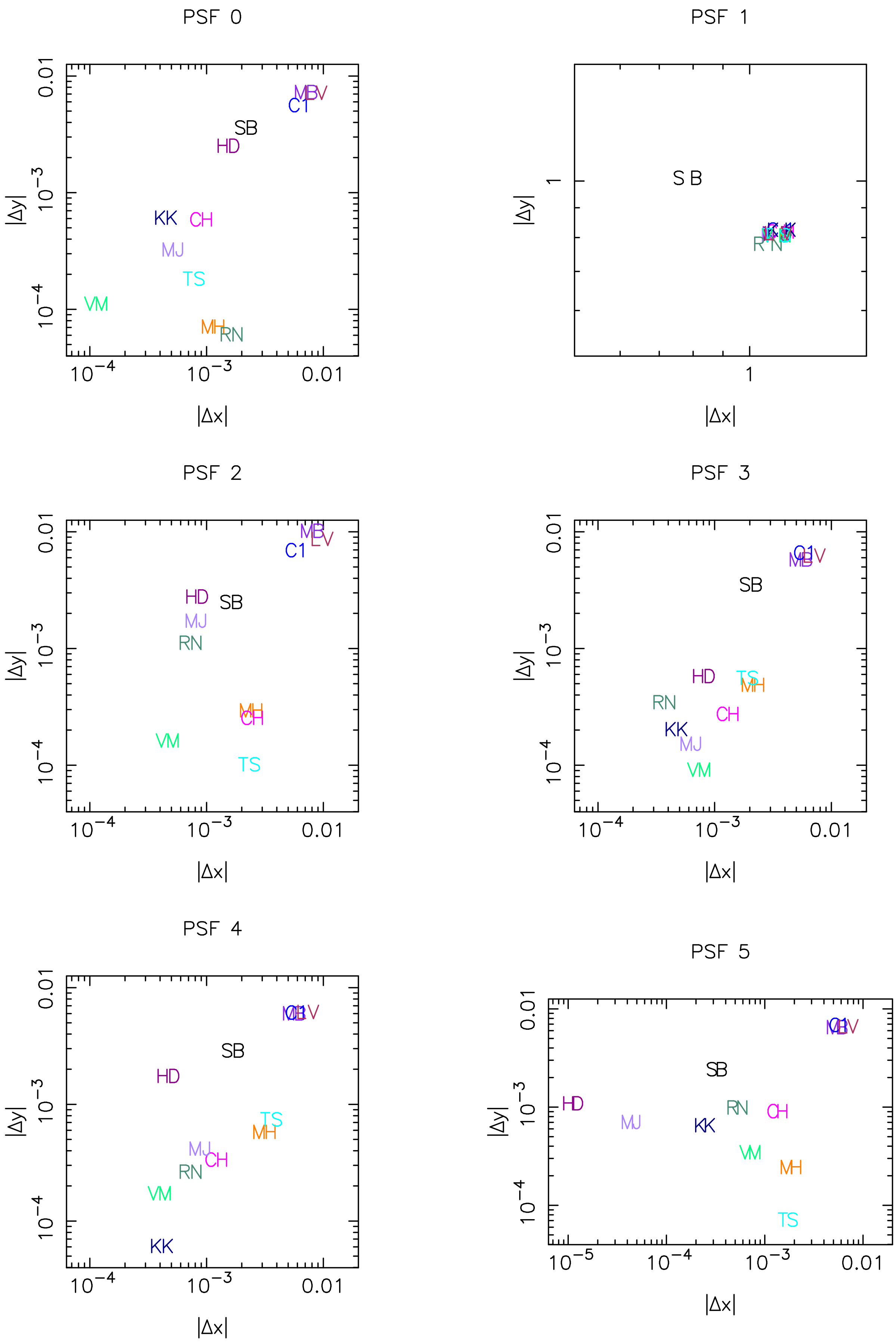

Figure 4: Centroids determined by source extraction software are compared to the positions of the input galaxies for different PSFs (external shear $\gamma = 0.01$). For most authors centroiding is good to 0.001 of a pixel except in the case of PSF 1 where most authors are ~ 1 pixel off. Note for the Brown (MB) and Clowe (C1&2) pipelines that use *hfindpeaks*, 0.5 pixels has been added to the measured centroids.

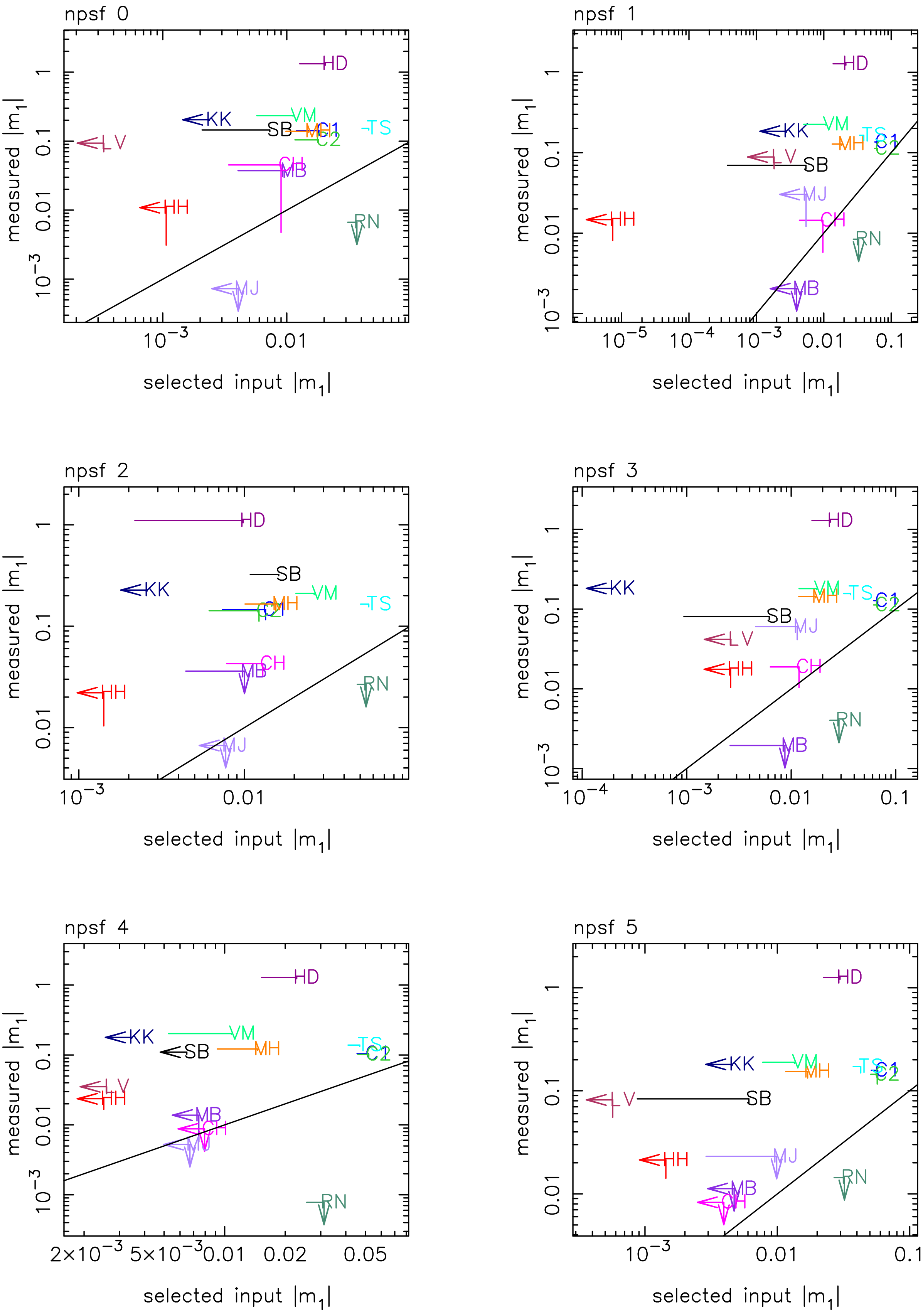

Figure 5: Selection bias compared to measured calibration bias for all PSF types. The best fitting values for m_1 (equation 1), are determined using unweighted input galaxy shear parameters (x axis) and measured galaxy shear parameters for 'real' galaxies (y axis). Errors are plotted in the direction that reduces m to zero except in the cases when parameters are consistent with zero where an arrow is shown. With unbiased measurement methods, points should fall along the 1:1 line plotted

3.4 Weight bias

The methods of Bridle (SB), Clowe (C1&2), Hetterscheidt (MH), Hoekstra (HH), Kuijken (KK), Schrabback (TS) and Van Waerbeke (LV) employ a shear weighting scheme. In this section we investigate the impact of these weights by comparing the unweighted and weighted shear measured using the selected input galaxy shears and the author defined weights. Note that the input galaxy shear is defined by equation 3. An optimal weighting scheme reduces the noise on a measurement without biasing the results. Any weight bias, for example the downweighting of highly elliptical objects, will bias the mean shear of the population.
Figure 6 compares the offset parameter m_1 from equation 1 measured for the same set of selected galaxies using unit weights (x axis) and author defined weights (y axis). **With unbiased weights, points should be consistent with zero or fall along the 1:1 line plotted.** Note the unweighted results reproduce the selection bias results discussed in section 3.3. We find unbiased weights with all methods except with the methods of Hetterscheidt (MH) and Schrabback (TS) where the weights (see table 6 for a weight prescription) are found to significantly bias the result to lower shear values. A similar weighting scheme by Clowe (C1&2) is however unbiased. For the Kuijken (KK) method, selection bias and weight bias are consistent with zero for all PSF types and as such the $> 10\%$ calibration bias measured from the simulations must arise from a measurement bias.

3.5 Shear measurement dependence on magnitude, size and r_g

In this section we investigate the dependence of shear measurements on the input galaxy magnitude and the input galaxy disk-size. For authors who use KSB we also measure the dependence of shear measurement on the KSB scale size r_g (see section 5). Table 5 summarises the supplementary material `mag_bin.ps`, `disk_bin.ps` and `rg_bin.ps`, where we measure $\gamma_1 - \gamma_1^{\rm true}$, binned as a function of magnitude, disk size and r_g respectively for PSF 5 and $\gamma_1^{\rm true} = 0.1$. Table 5 details the magnitude, disk size, and r_g bins where the average binned shear was found to be more than 2σ away from the overall average. This shows that different methods have very different dependencies on galaxy properties, and that all KSB methods are very dependent on the scale size r_g that is used to measure weighted ellipticities.

4 Analysis of the shapelet simulations

In this section we present the analysis of the shapelet simulations, where realistic galaxy morphology are included in the image simulations. These have been analysed by a subset of the authors listed in table 1. We measure (weighted) quantities from each simulations and assign and error equal to 1 standard deviation or, in the cases where authors use weights, $\sigma^2 = 1/\Sigma(w)$. We use the same analysis technique as in section 3 fitting linear relationships to $\gamma - \gamma^{\rm true}$ as a function of the input shear for different PSFs to measure calibration bias and PSF contamination.

$$\gamma_i - \gamma_i^{\rm true} = m_i \gamma_i^{\rm true} + c_i \tag{4}$$

In the case where $\gamma_i^{\rm true}$ is equal to zero for the whole PSF set we fit to $\gamma_j^{\rm true}$. The supplementary `shapelets_analysis.ps` shows the difference between the measured shear and the true shear for each PSF type and each author. Figures 7 and 8 show the best fitting value for m_1, c_1, m_2 and c_2, for PSF types 1-3, and PSF types 4 and 5 respectively. Again, **the lower the result on the y axis, the lower the level of calibration bias, and the further the result is placed to the left, the lower the level of PSF contamination**. When the fitted parameters are found to be consistent with zero an

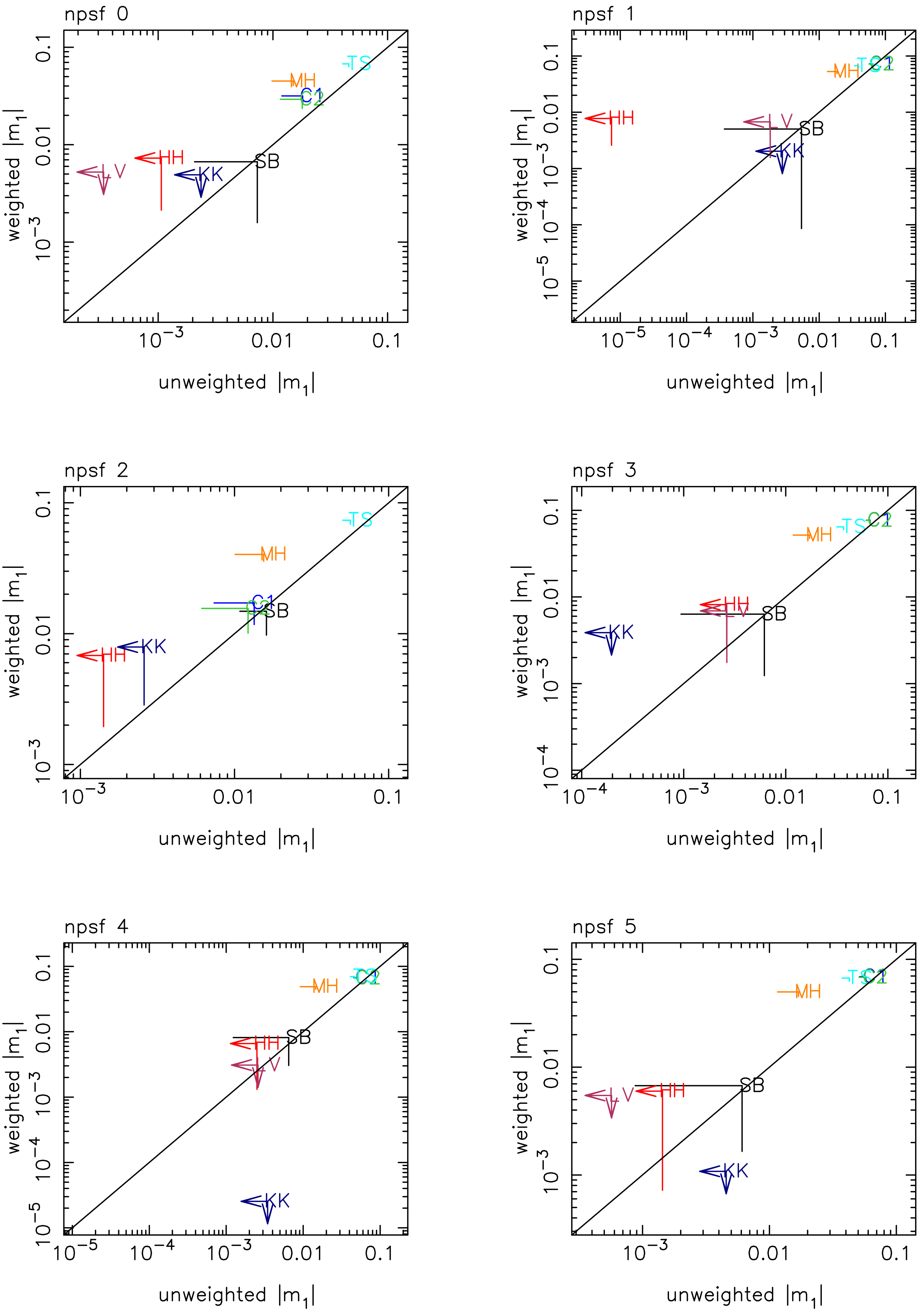

Figure 6: Comparing weighted and unweighted shear measurements for all PSF types; the best fitting values for m_1 (equation 1), measured using unweighted and weighted input galaxy shear parameters where the weights and selection criteria are defined by each author. Errors are plotted in the direction that reduces m to zero except in the cases when parameters are consistent with zero where an arrow is shown. With unbiased weights, points should fall along the 1:1 line plotted.

Author	Magnitude	Disk Length	KSB r_g
SB	$19 < R < 22$	$0.4 < d < 0.6$	-
MB	$R > 21$	$0.2 < d < 0.7$	$r_g \leq 3$, $r_g \geq 5$
C1	$R = 19$	$d < 0.2$	$r_g = 5$
C2	none	$d < 0.2$	$r_g = 5$
HD	Yes - no trend	bias inc with inc d	-
MH	$20 < R < 22$	$0.4 < d < 0.6$	$r_g \leq 3$
CH	none	none	$r_g \leq 3$, $r_g \geq 5.5$
HH	$21 < R < 23$	none	$3 \leq r_g \geq 4$
MJ	$R = 21$	$d < 0.5$	-
KK	$R > 20$	$d < 0.2$, $d = 0.5$	-
VM	$21 < R < 23$	$0.2 < d < 0.5$	-
RN	$20 < R < 22$	$d < 0.5$	-
TS	$R = 21$	none	$r_g \leq 3$, $r_g \geq 5$
LV	$R = 21$	none	full $r_g$range

Table 5: The dependence of shear as a function of magnitude, disk size and r_g for PSF 5 and $\gamma_1^{\rm true} = 0.1$. The entries detail the magnitude, disk size, and r_g bins where the average binned shear was found to be more than 2σ away from the overall average.

arrow is shown, otherwise errors on the fits are shown in the direction of the best case scenario of lower calibration bias, and lower PSF contamination.

The shapelet simulations contain fewer stars and fewer galaxies so we find a higher level of PSF contamination and a higher level of shot noise. Again we find calibration bias in some but not all methods with the Heymans (CH) method faring well with a calibration bias consistent with zero for all PSF distortions (in contrast to often the poorest PSF removal). Comparing the calibration bias seen with the KSB-based Gray (MG) and Brown (MB) method is interesting in light of the fact that these pipelines stem from the Bacon KSB pipeline. Gray (MG) in contrast to Brown (MB) does not include the Bacon calibration factor which would reduce this bias by $\sim 20\%$. PSF correction is typically better than the percent level, with PSF 3 causing the most problems. This PSF is particularly nasty and it is likely that data with such a PSF would be rejected from a cosmic shear survey.

A comparison of these results with those from the SkyMaker simulations is difficult owing to the different noise properties in the results. To understand the differences seen it will be necessary to analyse more shapelet simulations with the same area, galaxy density and stellar density as the SkyMaker simulations. It is however interesting to note that most methods do not fare as well with the shapelet simulations. It is unclear whether this is a result of the poorer PSF correction owing to the lower number density of stars, or whether it is a result of the PSF and galaxy ellipticity variation as a function of radius. This variation is in principle taken into account in the Heymans (CH) and Schrabback (TS) pipeline by creating PSF models as a function of r_g.

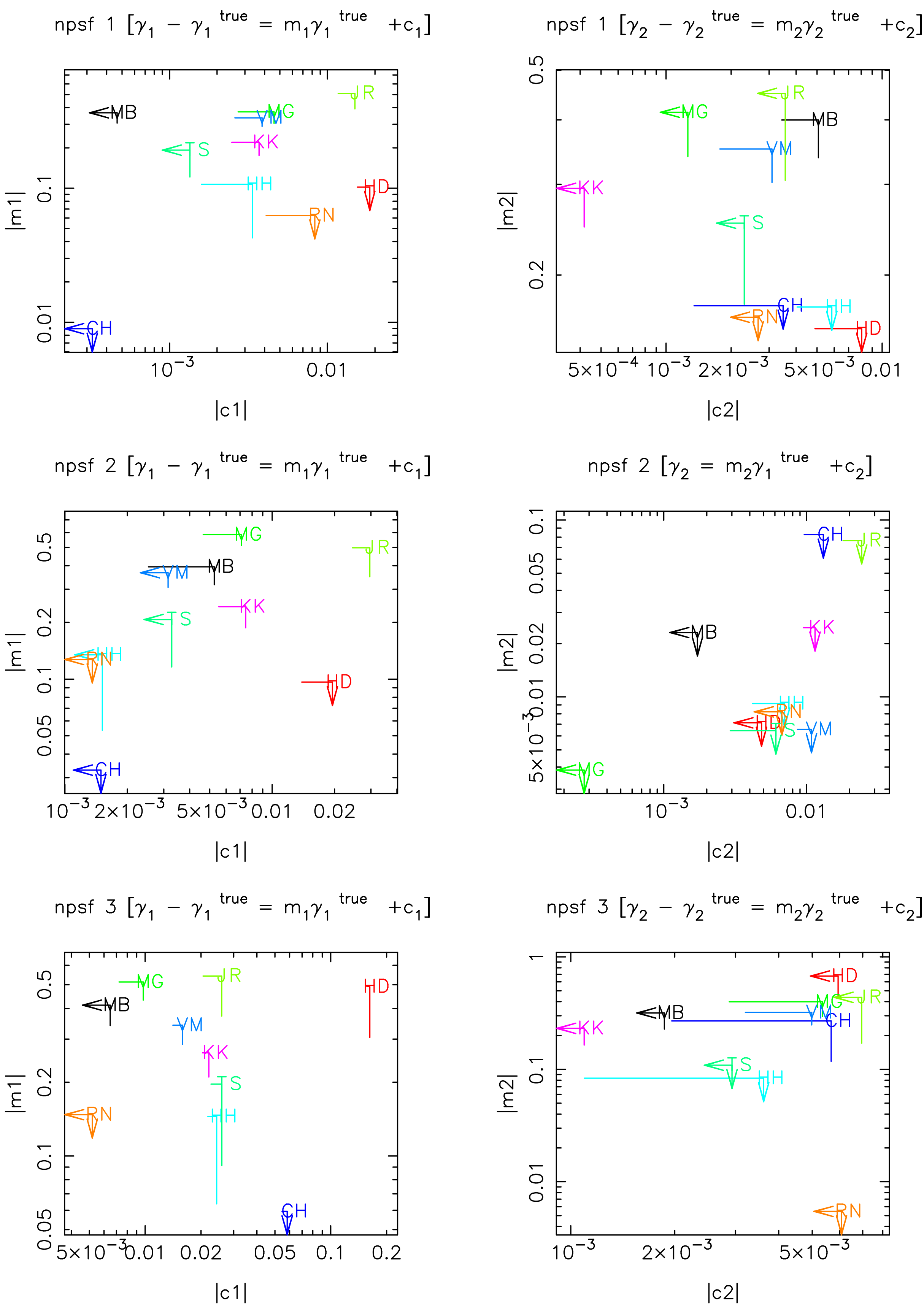

Figure 7: Shapelet simulations: The best fitting values for m_i and c_i (equation 4) for each author (key listed in table 1), for shapelet PSF types 1-3. Errors are plotted in the direction that reduces m_i and c_i to zero except in the cases when parameters are consistent with zero where an arrow is shown.

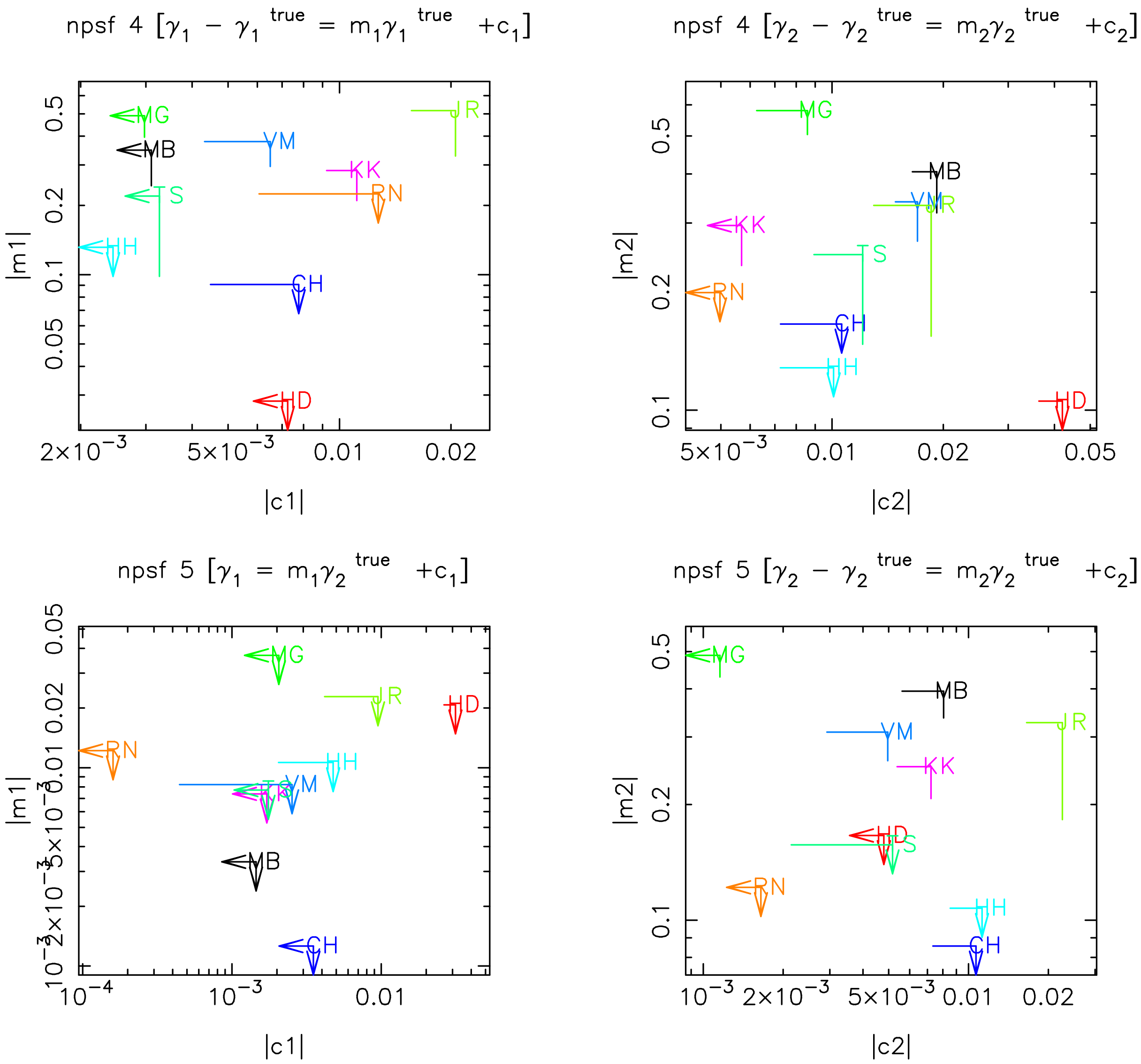

Figure 8: Shapelet simulations: The best fitting values for m_i and c_i (equation 4) for each author (key listed in table 1), for shapelet PSF types 4-5. Errors are plotted in the direction that reduces m_i and c_i to zero except in the cases when parameters are consistent with zero where an arrow is shown.

5 KSB analysis

Kaiser et al. [1995], Luppino and Kaiser [1997] and Hoekstra et al. [1998] (KSB) prescribe a method to invert the effects of the PSF smearing and shearing, recovering an shear estimator uncontaminated by the systematic distortion of the PSF. This method has been used by a large percentage of the authors so we briefly review the formalism of the KSB method and then detail how different authors have implemented this method with their weak lensing pipelines, as summarised in table 6.
Objects are parameterised according to their weighted quadrupole moments

$$Q_{ij} = \frac{\int d^2\theta W(\theta) I(\theta)\, \theta_i \theta_j}{\int d^2\theta W(\theta) I(\theta)}, \tag{5}$$

where I is the surface brightness of the object, θ is the angular distance from the object centre and W is a Gaussian weight function of scale length r_g, where r_g is some measurement of galaxy size. For a perfect ellipse, the weighted quadrupole moments are related to the weighted ellipticity parameters ε_α by

$$\begin{pmatrix} \varepsilon_1 \\ \varepsilon_2 \end{pmatrix} = \frac{1}{Q_{11} + Q_{22}} \begin{pmatrix} Q_{11} - Q_{22} \\ 2Q_{12} \end{pmatrix}. \tag{6}$$

Kaiser et al. [1995] show that if the PSF distortion can be described as a small but highly anisotropic distortion convolved with a large circularly symmetric Gaussian, then the ellipticity of a PSF corrected galaxy is given by

$$\varepsilon_\alpha^{\rm cor} = \varepsilon_\alpha^{\rm obs} - P^{\rm sm}_{\alpha\beta} p_\beta, \tag{7}$$

where p is a vector that measures the PSF anisotropy, and $P^{\rm sm}$ is the smear polarisability tensor given in Hoekstra et al. [1998]. $p(\theta)$ can be estimated from images of stellar objects at position θ by noting that a star, denoted throughout this report with *, imaged in the absence of PSF distortions has zero ellipticity: $\varepsilon_\alpha^{*\rm cor} = 0$. Hence,

$$p_\mu = (P^{\rm sm*})^{-1}_{\mu\alpha}\, \varepsilon_\alpha^{*\rm obs}. \tag{8}$$

The isotropic effect of the atmosphere and weight function can be accounted for by applying the pre-seeing shear polarisability tensor correction P^γ, as proposed by Luppino and Kaiser [1997], such that

$$\varepsilon_\alpha^{\rm cor} = \varepsilon_\alpha^s + P^\gamma_{\alpha\beta}\gamma_\beta. \tag{9}$$

where ε^s is the true source ellipticity and γ is the pre-seeing gravitational shear. Luppino and Kaiser [1997] show that

$$P^\gamma_{\alpha\beta} = P^{\rm sh}_{\alpha\beta} - P^{\rm sm}_{\alpha\mu}\,(P^{\rm sm*})^{-1}_{\mu\delta}\, P^{\rm sh*}_{\delta\beta}, \tag{10}$$

where $P^{\rm sh}$ is the shear polarisability tensor given in Hoekstra et al. [1998] and $P^{\rm sm*}$ and $P^{\rm sh*}$ are the stellar smear and shear polarisability tensors respectively. Combining the PSF correction, equation (7), and the P^γ seeing correction, the final KSB shear estimator $\hat\gamma$ is given by

$$\hat\gamma_\alpha = (P^\gamma)^{-1}_{\alpha\beta}\left[\varepsilon_\beta^{\rm obs} - P^{\rm sm}_{\beta\mu} p_\mu\right]. \tag{11}$$

5.1 Source Detection and Size definitions

Objects are detected either using the *SExtractor* software or *hfindpeaks* as discussed in section 3.2. The Gaussian weight scale length r_g is then either set to the `flux_radius` *SExtractor* parameter or the 'optimal' r_g value defined by *hfindpeaks*. Clowe (C1&2) uses both pieces of software using a version of *hfindpeaks* to determine the optimal weight scaling r_g that keeps the centroid fixed to the *SExtractor* co-ordinates. ε, $P^{\rm sm}$ and $P^{\rm sh}$ are then calculated for each object using various hacked versions of the *imcat* subroutine *getshapes*.

Table 6: Methods used by different authors to implement the KSB formalism described in section 5.

KSB Author	Brown	Clowe	Gray	Hetterscheidt	Heymans	Hoekstra	Schrabback	Van Waerbeke
Key	MB	C1&2	MG	MH	CH	HH	TS	LV
Source Detection	hfind	SExt + hfind	hfind	SExt	SExt	hfind	SExt	SExt
PSF: 2D polynomial model	2^{nd} order to ε^* and P^{sm*}, P^{sh*}	3^{rd} order to $\varepsilon^*, P^{sm*}, P^{sh*}$ C2: $(P^{sh}/P^{sm})(r_g)$	2^{nd} order to ε^* and P^{sm*}, P^{sh*}	3^{rd} order to $p^{\mu}(r_g^*)$ 3.5σ clipping	2^{nd} order to $p^{\mu}(r_g)$ and $(P^{sm*})^{-1}_{\alpha\beta} P^{sh*}_{\beta\gamma}(r_g)$		3^{rd} order to $p^{\mu}(r_g)$ and $(P^{sm*})^{-1}_{\alpha\beta} P^{sh*}_{\beta\gamma}(r_g)$	2^{nd} order
Galaxy size r_g	from hfind	from hfind	from hfind	flux_radius	flux_radius	from hfind	flux_radius	flux_radius
P^{γ} correction	Fit of $\frac{1}{2}Tr(P^{\gamma})(r_g)$	Fit $P^{\gamma}_{ii}(r_g, e)$ C1:$(P^{sh}/P^{sm})(r_g^*)$ C2:$(P^{sh}/P^{sm})(r_g)$	Fit binned $\frac{1}{2}Tr(P^{\gamma})(r_g)$	$\frac{1}{2}Tr(P^{\gamma})$ (no fit)	$\frac{1}{2}Tr(P^{\gamma})(r_g)$ (no fit)	Fit of $\frac{1}{2}Tr(P^{\gamma})(r_g)$	$\frac{1}{2}Tr(P^{\gamma})(r_g)$ (no fit)	Fit in (r_g, mag) to $\frac{1}{2}Tr(P^{\gamma})$
Weights	none	$\frac{1}{<\gamma^2>(r_g,\nu)}$	none	$\frac{1}{<\gamma^2>(r_g,mag)}$	none	Hoekstra et al. eqn A8,9	$\frac{1}{<\gamma^2>(r_g,mag)}$	Hoekstra et al. eqn A8,9
Ellipticity cut Size cut Significance cut P^{γ} cut γ cut Other	$\|\varepsilon_{obs}\| \leq 0.5$ $r_g > r_g^*$ $\nu > 5$	 $r_g^* < r_g < 6$ px $\nu > 10$ $P^{\gamma}_{ii} \geq 0.15$ $\|d\| < 1$px SEx class <0.8 No sat/bad px $3r_g$ of centroid	$\|\varepsilon_{obs}\| \leq 0.5$ $r_g > r_g^*$ $\nu > 5$ $P^{\gamma}_{model} > 0.1$ $\|\gamma\| < 2$	$\|\varepsilon_{obs}\| \leq 0.8$ $r_g > r_g^*$ $\frac{1}{2}Tr(P^{\gamma}) > 0$	$\|\varepsilon_{obs}\| \leq 0.5$ $1.2r_g^* < r_g < 7$px $\nu > 10$ $\|\gamma\| < 2$ Close pairs < 10px removed		$\|\varepsilon_{cor}\| \leq 0.8$ $r_g > 1.2r_g^*$ $\frac{1}{2}Tr(P^{\gamma}) > 0$	 $\nu > 15$

5.2 Anisotropic PSF modelling

Stellar objects are selected by eye from the stellar locus in a size-magnitude plane and are then used to produce a polynomial model of the PSF as a function of chip position. Brown (MB), Clowe (C1&2) and Gray (MG) create models of $\varepsilon_\alpha^{*obs}$, P^{sm*} and P^{sm*} separately. Hetterscheidt (MH), Heymans (CH) and Schrabback (TS) fit directly to p_μ which, in the case of Heymans (CH) and Schrabback (TS), is measured for varying r_g [Hoekstra et al., 1998]. This is in contrast to Brown (MB), Gray (MG), Hetterscheidt (MH) and the first Clowe method (C1) where stellar shapes are measured with $r_g = r_g^*$. With PSF models in hand observed galaxy ellipticities are corrected according to equation 7.

5.3 Isotropic P^γ correction

The application of the anisotropic PSF correction leaves an effectively isotropic distortion making objects rounder as a result of both the PSF and the Gaussian weight function used to measure the galaxy shapes. To correct for this effect and convert weighted galaxy ellipticities ε into unbiased shear estimators $\hat{\gamma}$, we use the pre-seeing shear polarisability tensor P^γ, equation (10). P^γ is calculated for each galaxy from the measured galaxy smear and shear polarisability tensors, $P^{\rm sm}$ and $P^{\rm sh}$, and a term that is dependent on stellar smear and shear polarisability tensors; $(P^{\rm sm*})^{-1}_{\mu\delta} P^{\rm sh*}_{\delta\beta}$. Brown (MB), Gray (MG) and the first method of Clowe (C1) use the stellar smear and shear polarisability tensors measured with a Gaussian weight of scale size $r_g = r_g^*$. Hetterscheidt (MH), Heymans (CH), Schrabback (TS) and the second method of Clowe (C2) calculate this stellar term as a function of smoothing scale r_g. Comparing the C1 and C2 results therefore demonstrates the impact of the inclusion of scale size at this stage.
P^γ is a very noisy quantity, especially for small galaxies. This noise is reduced somewhat by treating P^γ as a scalar equal to half its trace (note that the off diagonal terms of P^γ are typically very small). In an effort to reduce the noise on P^γ still further, P^γ is often fit as a function of r_g, see Table 6 for details, and in the case of Clowe (C1&2), P^γ is also fit as a function of ε.

5.4 Weights

Some authors employ a weighting scheme in their analysis. Hoekstra (HH) uses weights based on the error in the ellipticity measurement. These weights are derived in Appendix A1 of Hoekstra et al. [2000]. Clowe (C1&2) and Hetterscheidt (MH) and Schrabback (TS) use a weighting scheme based on the inverse of $< \gamma^2 >$ for all galaxies within a given amount of r_g and magnitude (TS) or significance ν (C1&2) of the galaxy using a minimum of 20/50 (TS,MH/C1&2) galaxies.

5.5 Selection criteria and calibration correction

After applying the KSB formalism to the data each author has included a set of selection criteria, listed in table 6, based on object significance, size, ellipticity, measured shear, measured(modelled) P^γ and so on. Brown (MB) also includes a calibration correction $\gamma_{cor} = \gamma/0.85$ as suggested from the analysis of image simulations in Bacon et al. [2001].

6 Alternatives to KSB

In this section we briefly review the alternative methods to KSB that have been used in this analysis.

6.1 K2K

One drawback of KSB is that for non-Gaussian PSF distortions, the KSB PSF correction is mathematically poorly defined. Kaiser [2000] (K2K) addresses this issue by properly accounting for the

effects of a realistic PSF. It also proposes measuring shapes from images that have been convolved with a re-circularising PSF. Section 2.3.6 of Dahle et al. [2002] provides a condensed description of the K2K shear estimator which has been applied to the STEP simulations by Dahle (HD). The Dahle (HD) results appear noisier than other pipelines which could result from an upper significance cut in order to remove big, bright 'unlensed' galaxies, which rejects $\sim 24\%$ of the objects. The method is optimised for mosaic CCD data with a high number of galaxies for each exposure, it therefore suffers somewhat from the low number of objects in each 4096×4096 STEP image. In addition, as a space-saving measure, images were stored in integer format, this may have introduced some extra noise in the 're-circularised' images.
In considering the success of K2K applied to STEP simulations we should keep in mind that the man-hours invested in testing and fine-tuning KSB is at least an order of magnitude more than for any of the other methods. In the case of K2K, little effort has been made so far to optimise some of the parameters, both due to lack of time and lack of an extensive, realistic simulated data set such as the simulations analysed here. With the STEP simulations future tests and optimisation are now feasible.

6.2 Rhodes, Refregier and Groth Method

Rhodes et al. [2000] builds on and develops the KSB formalism, showing that both the PSF and the camera distortions can be corrected for using source moments (equation 5), as opposed to ellipticities (equation 6). By decomposing the moments into spinors, an explicit relation between the shear and the average ellipticity is found. This method has been optimised for and used only on space-based data. The performance with ground-based simulations is therefore not necessarily a reflection of the performance with space-based data.

6.3 Bernstein and Jarvis Method

Bernstein and Jarvis [2002] provides a detailed description of the method that Jarvis (MJ) and Nakajima (RN) have applied to the STEP simulations. The steps of this analysis include measurement of object shapes on images, estimating the underlying shear from an ensemble of galaxy shapes, and compensating for the systematic effects of image distortion, bias from PSF asymmetries, and 'dilution' of the signal by the seeing. Galaxy images and PSFs are decomposed into a family of orthogonal 2D Gaussian-based functions making the PSF correction and shape measurement relatively straightforward and computationally efficient. This method is similar to the Shapelets method described below.

6.4 Shapelets

Based on the shapelet function formalism presented in Refregier [2003], galaxy images are decomposed into a series of localised basis functions of different shapes called 'shapelets'. The unique properties of shapelets under distortion provides estimates of the local shear. The formalism also allows for efficient modelling and deconvolution of the point spread function [Refregier and Bacon, 2003]. Kuijken (KK) has implemented this method on STEP simulations using shapelet coefficients up to 8^{th} order. The Cartesian shapelet formalism of Refregier [2003] has recently been extended to a polar shapelet formalism in Massey and Refregier [2004] and an accompanying IDL software package has been made available at `www.astro.caltech.edu/~rjm/shapelets`. This package has however been optimised for space-based data and requires some modifications before it can be applied to the ground-based STEP simulations.

6.5 Wittman method

Objects are detected with the *SExtractor* software, where the parameters are listed in table 4. *SExtractor* centroids and moments are then input to the *ellipto* program [Smith, 2000, Smith et al., 2001] which measures the 'adaptive' moments (moments weighted by the best-fit elliptical Gaussian). *ellipto* also re-measures the centroid and outputs an error flag if its centroid differs from the *SExtractor* centroid, which often happens with blended objects or those with nearby neighbours. Stars are selected with an automatic routine which looks for a dense locus at a constant *ellipto* size. The selection is then visually checked on a mag-size plot. For both the STEP simulations and real data, a few ($\sim 5\%$) of the images require manual tweaking of the star selection. The spatial variation of the adaptive moments is then fit with a second-order polynomial for each CCD of each exposure. This fit is then used to generate a 3×3 pixel kernel which, after convolution with the image, results in a circular PSF [Fischer and Tyson, 1997].

The PSF circularisation is checked by running *ellipto* on the convolved image and measuring the mean ellipticity components of the stars. If they are non-zero, the process is repeated. This happens for very elliptical input data which the 3x3 kernel can't handle in one pass. For the STEP simulations, only one PSF required this. Note, for real data, one pass is performed before stacking multiple exposures, and one pass is performed after. *ellipto* is run on the final image followed by a correction for dilution by an isotropic PSF using the formula of Bernstein and Jarvis [2002]. For this correction, a second-order fit to the spatial variation of the PSF size is used. The responsivity correction of Bernstein and Jarvis [2002] $(1- < e^2 >)$ of order $\sim 10\%$ has not been applied in this analysis and could therefore be the cause of the calibration bias found with the Margoniner (VM) result. This does not however affect the result of Wittman et al. [2000] because the dilution correction in this analysis was performed differently.

The final catalogue undergoes the following selection criteria where objects are rejected if: *SExtractor* flag > 3; non-zero *ellipto* error; measured (pre-dilution-correction) scalar ellipticity > 0.6 (simulations show that, with ground-based seeing, most of these are blends of unrelated objects); and size $< 120\%$ of the PSF size. Weighting is not applied to the data.

7 Conclusion

The Shear TEsting Programme analysis of sheared simulations has produced some very positive results with some methods producing results accurate at the percent level. As far as possible, details of each pipeline has been given in order to aid the future improvement of all methods in the hope that all future methods will reach the the best accuracy achieved in this analysis. The removal of the PSF distortion has been successful in all methods, at the percent level, with often negligible contamination in the cases of simple PSF distortions. Significant calibration bias is however seen in the results of some methods. For Clowe (C1&2), Hetterscheidt (MH) and Schrabback (TS) this $> 8\%$ bias can be explained, at least in part, by the use of biased weights and/or selection bias. For several methods selection bias is well below the percent level from which we can conclude that current source detection methods are suitable for weak lensing analyses and that any selection bias seen with other methods has been introduced after the source extraction stage. Centroid errors are small with *SExtractor* centroids accurate to ~ 0.001 pixels and *hfindpeaks* centroids accurate to ~ 0.01 pixels. Both types of source detection software used have however detected objects that are not included in the simulations, where the typical proportions of stellar contamination and false detections is at the 5% level. In some cases these false detections weakly dilute the signal but for some authors the false detections give a non-negligible signal. Different methods exhibited different dependences on galaxy magnitude and size. For real data where shear scales with depth and hence magnitude, these issues will need to be addressed.

The upcoming new generation of wide-area cosmic shear surveys will produce a significant reduction in shot noise when compared to current cosmic shear analyses. As such, the limiting error could soon result from simple uncertainties amongst the current suite of cosmic shear measurement methods. The collective goal of the cosmic shear community is to achieve high precision results that are competitive with other cosmological probes and STEP is certainly a necessary step towards reaching this goal. In this report we have shown that indeed some methods are accurate to the desired percent level and conclude with the hope that by using the shared technical knowledge compiled for this report, all future cosmic shear methods will be able to measure weak lensing to a high degree of accuracy.

8 Acknowledgments

We thank TERAPIX (Traitement Élémentaire, Réduction et Analyse des PIXels de megacam) at the Institut d'Astrophysique de Paris for hosting the SkyMaker simulations, and the Department of Astronomy at CALTECH for hosting the shapelet simulations.

References

D. J. Bacon, A. Refregier, D. Clowe, and R. S. Ellis. Numerical simulations of weak lensing measurements. *MNRAS*, 325:1065–1074, August 2001.

M. Bartelmann and P. Schneider. Weak gravitational lensing. *Physics Reports*, 340:291, 2001.

G. M. Bernstein and M. Jarvis. Shapes and Shears, Stars and Smears: Optimal Measurements for Weak Lensing. *AJ*, 123:583–618, February 2002.

E. Bertin and S. Arnouts. SExtractor: Software for source extraction. *A&AS*, 117:393–404, June 1996.

S. Bridle, S. Gull, S. Bardeau, and J. P Kneib. The Shapes of Galaxies and their Dark Halos. In N.P World Scientfic, editor, *Proceedings of the Yale Cosmology Workshop*, 2001.

M. Brown, A.N. Taylor, D.J. Bacon, M. Gray, S. Dye, K. Meisenheimer, and C. Wolf. The shear power spectrum from the COMBO-17 survey. *MNRAS*, 341:100, 2003.

R. Crittenden, R. Natarajan, U. Pen, and T. Theuns. Discriminating weak lensing from intrinsic spin correlations using the curl-gradient decomposition. *ApJ*, 568:20, 2002.

H. Dahle, N. Kaiser, R. J. Irgens, P. B. Lilje, and S. J. Maddox. Weak Gravitational Lensing by a Sample of X-Ray Luminous Clusters of Galaxies. I. The Data Set. *ApJS*, 139, April 2002.

T. Erben, L. Van Waerbeke, E. Bertin, Y. Mellier, and P. Schneider. How accurately can we measure weak gravitational shear? *A&A*, 366:717–735, February 2001.

P. Fischer and J. A. Tyson. The Mass Distribution of the Most Luminous X-Ray Cluster RXJ 1347.5-1145 From Gravitational Lensing. *AJ*, 114:14–24, July 1997.

C. Heymans, M. L Brown, M. Barden, J. A. R. Caldwell, K. Jahnke, 'H.-W' Rix, A. N. Taylor, S. V. W. Beckwith, E. F. Bell, A. Borch, B. Häußler, S. Jogee, D. H. McIntosh, K. Meisenheimer, C. Y. Peng, S. F. Sanchez, R. S. Somerville, L. Wisotzki, and C. Wolf. Cosmological weak lensing with the HST GEMS survey. *MNRAS submitted, astroph/0411324*, 2004.

C. Hirata and U. Seljak. Shear calibration biases in weak-lensing surveys. *MNRAS*, 343:459–480, August 2003.

H. Hoekstra, M. Franx, and K. Kuijken. Hubble Space Telescope Weak-Lensing Study of the z=0.83 Cluster MS 1054-03. *ApJ*, 532:88–108, March 2000.

H. Hoekstra, M. Franx, K. Kuijken, and G. Squires. Weak Lensing Analysis of CL 1358+62 Using Hubble Space Telescope Observations. *ApJ*, 504:636, September 1998.

H. Hoekstra, H. Yee, and M. Gladders. Constraints on Ω_M and σ_8 from weak lensing in RCS fields. *ApJ*, 577:595, April 2002.

M. Jarvis, G. Bernstein, B. Jain, P. Fischer, D. Smith, J.A. Tyson, and D. Wittman. Weak Lensing Results from the 75 Square Degree CTIO Survey. *ApJ*, 125:1014, 2003.

N. Kaiser. A new shear estimator for weak lensing observations. *ApJ*, 537:555, 2000.

N. Kaiser, G. Squires, and T. Broadhurst. A method for weak lensing observations. *ApJ*, 449:460–475, 1995.

G. A. Luppino and N. Kaiser. Detection of Weak Lensing by a Cluster of Galaxies at z = 0.83. *ApJ*, 475:20–+, January 1997.

R. Massey, D. Bacon, A. Refregier, and R. Ellis. An Enlarged Cosmic Shear Survey with the William Herschel Telescope. *MNRAS submitted, astroph/0404195*, 2004.

R. Massey and A. Refregier. Polar Shapelets. *MNRAS submitted, astroph/0408445*, 2004.

R. Massey, A. Refregier, C. J. Conselice, J. David, and J. Bacon. Image simulation with shapelets. *MNRAS*, 348:214–226, February 2004.

A. Refregier. Shapelets - I. A method for image analysis. *MNRAS*, 338:35–47, January 2003.

A. Refregier and D. Bacon. Shapelets - II. A method for weak lensing measurements. *MNRAS*, 338: 48–56, January 2003.

J. Rhodes, A. Refregier, N. R. Collins, J. P. Gardner, E. J. Groth, and R. S. Hill. Measurement of Cosmic Shear with the Space Telescope Imaging Spectrograph. *ApJ*, 605:29–36, April 2004.

J. Rhodes, A. Refregier, and E. J. Groth. Weak Lensing Measurements: A Revisited Method and Application to Hubble Space Telescope Images. *ApJ*, 536:79–100, June 2000.

P. Schneider, L. Van Waerbeke, M. Kilbinger, and Y. Mellier. Analysis of two-point statistics of cosmic shear : 1 estimators and covariances. *A&A*, 369:1, 2002.

D. R. Smith. *Ph.D. thesis, Univ. Michigan.*, 2000.

D. R. Smith, G. M. Bernstein, P. Fischer, and M. Jarvis. Weak-Lensing Determination of the Mass in Galaxy Halos. *ApJ*, 551:643–650, April 2001.

L. Van Waerbeke, Y. Mellier, and H. Hoekstra. Dealing with systematics in cosmic shear studies: new results from the Virmos-Descart survey. *A&A submitted, astroph/0406468*, 2004.

D. Wittman, J. Tyson, D. Kirkman, and I. Dell'Antonio abd G. Berstein. Detection of weak gravitational lensing distortions of distant galaxies by cosmic dark matter at large scales. *Nat*, 405:143, 2000.

A Appendix

npsf	shear ID	γ_1	γ_2
1	A	0.000	-0.044
1	B	0.040	0.000
1	C	stellar	field
1	D	0.000	0.039
1	E	0.000	0.023
1	F	0.000	-0.029
1	G	-0.004	0.000
1	H	-0.058	0.000
1	I	0.000	-0.060
1	J	0.051	0.000
1	K	-0.030	0.000
1	L	0.021	0.000
1	M	0.000	-0.005
2	A	0.027	0.000
2	B	-0.016	0.000
2	C	-0.008	0.000
2	D	0.031	0.000
2	E	0.060	0.000
2	F	-0.042	0.000
3	A	-0.021	0.029
3	B	0.014	-0.022
3	C	0.040	-0.012
3	D	-0.048	-0.035
3	E	0.036	0.002
3	F	0.005	0.031
4	A	0.029	0.005
4	B	-0.022	0.014
4	C	0.020	-0.021
4	D	-0.035	0.036
4	E	0.031	0.040
4	F	-0.012	-0.048
5	A	0.000	0.007
5	B	0.000	0.052
5	C	0.000	-0.052
5	D	0.000	0.034
5	E	0.000	-0.018
5	F	0.000	0.060

Table 7: Input shear values for the shapelet simulations

author	npsf	Ngals	SNR	% stars	% false	Source	$x - x_{\rm true}$	$y - y_{\rm true}$
SB	0	14	13.9	3	5	SExtr	-0.002 ± 0.002	0.004 ± 0.002
LB	0	14	13.7	7	7	hfind	-0.494 ± 0.001	-0.493 ± 0.001
C1	0	12	17.5	2	3	hfind	-0.494 ± 0.001	-0.494 ± 0.001
C2	0	12	16.9	2	3	hfind	-0.494 ± 0.001	-0.495 ± 0.001
HD	0	17	11.0	44	45	hfind	-0.499 ± 0.001	-0.498 ± 0.001
MH	0	14	20.8	3	4	SExtr	-0.001 ± 0.001	0.000 ± 0.001
CH	0	12	13.0	2	3	SExtr	-0.001 ± 0.001	0.001 ± 0.001
HH	0	16	16.7	10	11	hfind	-0.989 ± 0.001	-0.989 ± 0.001
MJ	0	9	32.3	0	4	SExtr	0.000 ± 0.001	0.000 ± 0.001
KK	0	12	25.0	4	4	SExtr	0.000 ± 0.001	0.001 ± 0.001
VM	0	13	22.2	4	4	SExtr	0.000 ± 0.001	0.000 ± 0.001
RN	0	9	35.7	0	1	SExtr	-0.001 ± 0.001	0.000 ± 0.001
TS	0	10	19.6	1	1	SExtr	-0.001 ± 0.001	0.000 ± 0.001
LV	0	13	20.0	0	0	hfind	-0.492 ± 0.001	-0.493 ± 0.001
SB	1	14	15.9	4	6	SExtr	0.756 ± 0.001	1.009 ± 0.001
LB	1	15	14.3	6	7	hfind	0.577 ± 0.001	0.310 ± 0.001
C1	1	10	18.5	2	3	hfind	0.593 ± 0.001	0.323 ± 0.001
C2	1	10	17.9	2	3	hfind	0.593 ± 0.001	0.322 ± 0.001
HD	1	17	14.1	46	47	hfind	0.579 ± 0.001	0.309 ± 0.001
MH	1	14	23.3	3	4	SExtr	1.073 ± 0.001	0.804 ± 0.001
CH	1	12	14.7	2	2	SExtr	1.089 ± 0.001	0.817 ± 0.001
HH	1	16	17.2	10	11	hfind	0.072 ± 0.001	-0.194 ± 0.001
MJ	1	10	38.5	0	4	SExtr	1.073 ± 0.001	0.804 ± 0.001
KK	1	12	25.6	2	3	SExtr	1.097 ± 0.001	0.822 ± 0.001
VM	1	15	24.4	7	7	SExtr	1.072 ± 0.000	0.804 ± 0.000
RN	1	11	43.5	0	1	SExtr	1.038 ± 0.001	0.778 ± 0.001
TS	1	12	23.8	1	1	SExtr	1.073 ± 0.001	0.804 ± 0.001
LV	1	13	20.0	0	0	hfind	0.581 ± 0.000	0.311 ± 0.000
SB	2	13	12.3	2	6	SExtr	-0.001 ± 0.002	0.002 ± 0.002
LB	2	13	15.9	6	7	hfind	-0.493 ± 0.001	-0.490 ± 0.001
C1	2	11	17.9	2	2	hfind	-0.495 ± 0.001	-0.493 ± 0.001
C2	2	11	17.9	2	2	hfind	-0.495 ± 0.001	-0.493 ± 0.001
HD	2	16	12.5	42	42	hfind	-0.499 ± 0.001	-0.497 ± 0.001
MH	2	13	23.3	4	4	SExtr	-0.002 ± 0.001	0.000 ± 0.001
CH	2	12	12.0	3	3	SExtr	-0.002 ± 0.001	0.000 ± 0.001
HH	2	15	19.6	11	11	hfind	-0.987 ± 0.001	-0.986 ± 0.001
MJ	2	8	33.3	0	3	SExtr	-0.001 ± 0.001	-0.002 ± 0.001
KK	2	11	27.0	7	7	SExtr	0.000 ± 0.001	0.000 ± 0.001
VM	2	12	20.0	8	8	SExtr	0.000 ± 0.001	0.000 ± 0.001
RN	2	7	29.4	1	2	SExtr	0.001 ± 0.001	-0.001 ± 0.001
TS	2	8	19.2	1	1	SExtr	-0.002 ± 0.001	0.000 ± 0.001

Table 8: Table to compare the different number density of detected sources per square arcmin and the percentage of false detections for PSFs 0,1 and 2 when the external shear $\gamma = 0.01$. Centroid offsets are also shown.

author	npsf	Ngals	SNR	% stars	% false	Source	$x - x_{\rm true}$	$y - y_{\rm true}$
SB	3	14	16.1	4	7	SExtr	-0.002 ± 0.001	0.003 ± 0.001
LB	3	15	15.2	5	6	hfind	-0.495 ± 0.001	-0.494 ± 0.001
C1	3	9	18.5	3	3	hfind	-0.495 ± 0.001	-0.493 ± 0.001
C2	3	9	18.2	3	3	hfind	-0.495 ± 0.001	-0.494 ± 0.001
HD	3	17	14.3	47	47	hfind	-0.499 ± 0.001	-0.499 ± 0.001
MH	3	15	25.6	4	4	SExtr	-0.002 ± 0.001	0.000 ± 0.001
CH	3	13	15.4	2	3	SExtr	-0.001 ± 0.001	0.000 ± 0.001
HH	3	16	16.1	9	10	hfind	-0.990 ± 0.001	-0.991 ± 0.001
MJ	3	10	31.2	0	3	SExtr	0.001 ± 0.000	0.000 ± 0.001
KK	3	12	23.8	2	2	SExtr	0.000 ± 0.000	0.000 ± 0.001
VM	3	14	21.7	4	5	SExtr	-0.001 ± 0.000	0.000 ± 0.000
RN	3	11	41.7	0	1	SExtr	0.000 ± 0.001	0.000 ± 0.001
TS	3	12	24.4	1	1	SExtr	-0.002 ± 0.001	-0.001 ± 0.001
LV	3	13	20.0	0	0	hfind	-0.494 ± 0.001	-0.494 ± 0.000
SB	4	14	14.1	4	6	SExtr	-0.002 ± 0.002	0.003 ± 0.002
LB	4	15	14.3	7	8	hfind	-0.495 ± 0.001	-0.494 ± 0.001
C1	4	10	16.7	2	3	hfind	-0.495 ± 0.001	-0.494 ± 0.001
C2	4	10	16.4	3	3	hfind	-0.495 ± 0.001	-0.494 ± 0.001
HD	4	17	15.2	46	47	hfind	-0.500 ± 0.001	-0.498 ± 0.001
MH	4	15	22.7	5	5	SExtr	-0.003 ± 0.001	-0.001 ± 0.001
CH	4	13	12.7	3	3	SExtr	-0.001 ± 0.001	0.000 ± 0.001
HH	4	16	15.9	10	10	hfind	-0.990 ± 0.001	-0.991 ± 0.001
MJ	4	10	32.3	0	4	SExtr	-0.001 ± 0.001	0.000 ± 0.001
KK	4	12	25.6	2	3	SExtr	0.000 ± 0.001	0.000 ± 0.001
VM	4	14	21.7	5	5	SExtr	0.000 ± 0.000	0.000 ± 0.000
RN	4	10	40.0	0	1	SExtr	-0.001 ± 0.001	0.000 ± 0.001
TS	4	11	21.7	1	1	SExtr	-0.003 ± 0.001	-0.001 ± 0.001
LV	4	13	13.9	0	0	hfind	-0.493 ± 0.001	-0.494 ± 0.000
SB	5	14	15.9	4	7	SExtr	0.000 ± 0.001	0.002 ± 0.001
LB	5	15	15.2	7	8	hfind	-0.495 ± 0.001	-0.494 ± 0.001
C1	5	10	19.2	3	3	hfind	-0.495 ± 0.001	-0.493 ± 0.001
C2	5	10	18.2	3	3	hfind	-0.495 ± 0.001	-0.493 ± 0.001
HD	5	17	13.9	47	47	hfind	-0.500 ± 0.001	-0.499 ± 0.001
MH	5	15	22.7	4	4	SExtr	-0.002 ± 0.001	0.000 ± 0.001
CH	5	13	12.2	3	3	SExtr	-0.001 ± 0.001	0.001 ± 0.001
HH	5	16	16.4	10	11	hfind	-0.990 ± 0.001	-0.991 ± 0.001
MJ	5	10	35.7	0	4	SExtr	0.000 ± 0.001	0.001 ± 0.001
KK	5	12	23.8	2	3	SExtr	0.000 ± 0.001	0.001 ± 0.001
VM	5	14	22.2	4	5	SExtr	-0.001 ± 0.000	0.000 ± 0.000
RN	5	11	40.0	0	1	SExtr	0.000 ± 0.001	-0.001 ± 0.001
TS	5	12	20.4	1	1	SExtr	-0.002 ± 0.001	0.000 ± 0.001
LV	5	13	19.6	0	0	hfind	-0.494 ± 0.001	-0.493 ± 0.000

Table 9: Table to compare the different number density of detected sources per square arcmin and the percentage of false detections for PSFs 3,4 and 5 when the external shear $\gamma = 0.01$. Centroid offsets are also shown.